Coupled finite/boundary element solution of magnetothermal problems

S.P. Song and B.Q. Li

Department of Mechanical Engineering, Louisiana State University, Baton Rouge, Louisiana, USA and

J.M. Khodadadi

Department of Mechanical Engineering, Auburn University, Auburn, Alabama, USA

Received October 1996
Accepted March 1997

Nomenclature

a = Radius of a sphere
$\vec{A}$ A,A* = Magnetic vector potential, its component, and complex conjugate
$\bar{A}$ = Global unknown nodal vector of vector potential
C = Geometric coefficient from BE formulation
C_p = Heat capacity
E(γ) = Elliptical integral of the second kind
F = Force vector
$\bar{F}$ = Global force vector of coupled FE-BE formulation
$\vec{G}$, G = Vector Green function and its component
H, **G** = Global coefficient matrices of BE formulation
I = Current (Peak value)
I_k = Modified Bessel function of the first kind of order k
$\vec{J}$, J = Current density and its component
k = System parameter for electromagnetic field
K = Thermal conductivity
K (*k*) = Elliptical integral of the first kind
K = Finite element global coefficient matrix
$\bar{\mathbf{K}}$ = Global coefficient matrix of coupled FE-BE formulation
M = FE-BE global matrix
N = Finite element boundary flux coefficient matrix
n = Outward normal
N = Number of boundary elements
N_e = Number of nodes per FE element
P_n^1 = Associated Legendre polynomials
q = Global normal derivative vector
r,r = Point vector and r coordinate
r_o = Radial distance of a single coil
S = Surface
t = Time
T = Temperature
u = Unknown vector
v = Volume
$\hat{z}$ = Unit vector of z-direction
z = z co-ordinate

Greek symbols

ν = Subtended angle of the exciting coil for single sphere system
α = Geometric angle around a corner of FE-BE interface
β = Angle between the outnormal and x-direction
$\vec{\delta}$ = Vector delta function
∇ = Gradient operator
Φ = Shape function
μ = Magnetic permeability
Π = Π-constant
$\hat{\theta}$ = Unit vector of θ-direction
σ = Electrical conductivity
ω = Frequency
Ω = Computational domain
∂Ω = Boundary of computational domain

Subscripts

1,2 = Finite and boundary element regions, respectively
e = Element
I = FE-BE interface
B = Boundaries excluding FE-BE interface
T = Temperature

Superscripts

* = Complex conjugate
T = Matrix transpose
n = The nth component

International Journal of Numerical Methods for Heat & Fluid Flow
Vol. 8 No. 3, 1998, pp. 321–349.

1. Introduction

Magnetothermal problems arise naturally during electromagnetic processing of electrically conducting materials. Examples can be cited from widely practiced industrial processes such as induction furnace[1-3], electromagnetic casting[4,5], magnetic suspension melting[6], floating zone crystal growth and zone refining[7], induction heating treatment[8] as well as important laboratory systems for materials property measurements such as magnetic levitation processes under both normal and micro gravity[9,10]. In these processes, heat transfer is profoundly affected by Joule heating that results from the interaction of eddy currents induced in the materials by an externally imposed alternating electromagnetic field.

Accurate prediction of the magnetothermal phenomena is of critical importance to the fundamental understanding of physical principles that govern the electrodynamics and thermal behavior of materials in these processing systems. For these purposes, many numerical algorithms have been developed and the effort is still continuing to satisfy the accuracy and efficiency demand for process design and analyses. A computational procedure of the solution of magnetothermal problems in general involves predicting the induced current density field based on the external electromagnetic field configuration, from which the Joule heating source is calculated. The Joule heating then serves as a distributed source for the calculation of the temperature distribution subject to thermal boundary conditions[11,12]. The computational schemes presently in use in general can be classified into three categories, that is, the finite element and finite difference methods and the boundary element method. The former two are domain based numerical algorithms while the latter is boundary based.

The finite element method, which has its root in variational calculus, is a very useful engineering numerical method for the solution of boundary value problems defined over irregular boundaries. The use of the method requires the discretization of the entire domain. The method can be applied to solve both linear and nonlinear problems, but is particularly powerful for nonlinear problems that involve the field variables defined within a computational domain[13]. On the other hand, the boundary element method, which permits formulation of field variables along the boundaries only, is very efficient for linear boundary value problems and for nonlinear problems with nonlinearity occurring along the boundaries[14-16]. The primary advantage of the boundary element method lies in the fact that only the boundaries of the computational domain need to be discretized, and hence the dimension of the problem is reduced by one, compared with the finite element method. Thus, if appropriately applied, the boundary element method can be computationally more efficient and also have an advantage of less data storage requirement[14].

The authors gratefully acknowledge the support of this work by the National Science Foundation (Grant No. NSF-CTS 9622275).

In problem analyses, it is often desirable to obtain detailed information on field distributions within only a certain part of the computational domain but not necessarily the entire one. This can be particularly true for magnetothermal calculations where the local Joule heating distribution is needed only for the conducting workpiece. When the finite element method is used for these problems, an entire domain, including both the workpiece and the space external to it, must be discretized, even though in almost all the cases the field distribution inside the workpiece itself is of interest only. Thus considerable computational time as well as large data storage space are used to account for the areas where information on field distribution is basically not needed. Although less popular for electromagnetic computations, the finite difference method, when applied, would encounter the same computational and storage problem. While the problem may be alleviated by applying the boundary element method, it alone would be cumbersome to apply, particularly in the conductor regions, because of either complicated Green's function evaluation or materials nonlinearity or both. For this class of problems, it is conceivable that a more appropriate computational algorithm would be to combine the domain-based method for the part of the domain in which information is desired, with other methods that are less computationally intensive to account for the other part of the domain. One of these choices would involve the coupling of finite element and boundary element methods by which finite elements are used for the regions of interest while boundary elements for the other regions[17]. The idea of coupling finite elements and boundary elements has been demonstrated for the solution of some solid mechanics and electromagnetic scattering problems[18-24]. There are also algorithms developed based on the coupling of the finite difference and boundary element methods for the solution of boundary value problems in materials processing systems[25]. It appears, however, that there has been very little, if any, published work on the development of coupled finite element and boundary element algorithms for the solution of magnetothermal problems, although the general concept has been tossed around for some time[17].

This paper presents a coupled finite element and boundary element computational methodology for the solution of magnetothermal problems. In what follows, the FE-BE formulation of the electrodynamic problems and the finite element formulation of heat transfer problems as related to magnetothermal phenomena is described, along with the detailed procedure for the implementation of the FE-BE coupling. Discussion is also made on the treatment of corners of both the FE-BE and BE regions, as inappropriate handling of these corners can introduce inaccuracy in numerical results. While case studies are made for 2-D and axisymmetric geometries, the formulation and computational procedure should be readily extended to 3-D problems. The derivation of vector Green's function for axisymmetric problems and its derivative are also presented, along with the calculation of the singular geometric coefficients associated with the boundary element formulation of vector potentials. Examples are given illustrating the algorithm for the

prediction of both the electromagnetic field and temperature distributions. The numerical results are compared with analytical solutions when available.

2. Problem statement

Let us consider the magnetothermal problem as illustrated in Figure 1. An electrically conducting specimen is surrounded by a current loop, through which an alternating current is imposed. By Faraday's law, eddy currents will be induced in the specimen and the self-interaction of the eddy current field represents the electric energy or Joule heating by which the workpiece is heated up. If the applied current is sufficiently high and/or the heating time is long enough, melting will occur resulting in liquid phase formation.

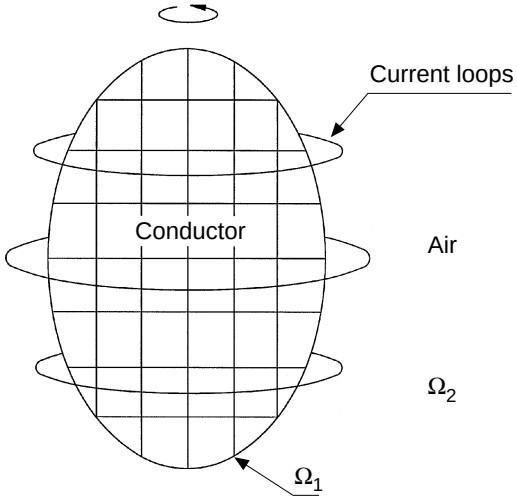

Figure 1.
Schematic representation of the finite element and boundary element solution of magnetothermal problems

A complete description of a magnetothermal problem would involve the solution of the Maxwell equations for the electrodynamic phenomena, the energy balance equation for temperature distribution and the Navier-Stokes equation for liquid flow if a fluid is present[11,12]. This represents a very complex nonlinear mathematical system. For the problems considered in this paper, the Joule heating source distribution generated by the surrounding coils will be predicted by a coupled finite element/boundary element (FE/BE) method and conduction is assumed to be the predominant mode of heat transfer. This should suffice to illustrate the usefulness of the computational method. For calculations involving solids only, the assumption of conduction is valid. For calculations involving liquids, however, a more accurate prediction of the thermal field would have to consider the liquid convection that is driven by both buoyancy and electromagnetic forces[12]. It is noted that the convection effect may be readily incorporated in light of the fact that the numerical computation of heat transfer and fluid flow has already been well established[26].

The first step involved in studying magnetothermal phenomena is to determine the induced electromagnetic field in the specimen surrounded by the exciting coils.

For induced field calculations, the complex Maxwell equation set can be written in terms of the magnetic vector potential. Also, for the electromagnetic field configurations encountered in induction processes, the low frequency approximation is often valid and thus the displacement current field can be safely ignored[11]. Thus for a harmonically oscillating magnetic field, the mathematical formulation for a magnetothermal problem, subject to the aforementioned assumptions, may be written in terms of a vector Helmholtz equation using a phasor notation for the vector potential $\vec{A}$[27,28],

$$\nabla^2 \vec{A} = k^2 \vec{A} - \mu \vec{J} \qquad \in \Omega_1 \cup \Omega_2 \tag{1}$$

$$\rho C_p \frac{\partial T}{\partial t} = \nabla K \bullet \nabla T + 0.5\omega^2 \sigma \vec{A} \cdot \vec{A}^* \qquad \in \Omega_1 \tag{2}$$

where k^2 (= $j\omega\mu\sigma$) is the system parameter and $\vec{J}$ the applied current. Note that equation (1) applies to both the inside and outside of the specimen, and when applied to the outside region, k = 0.

The physical constraints must be imposed as boundary conditions in order to solve the above governing equations. For the configurations as sketched in Figure 1, the tangential and normal components of the magnetic field must be continuous along the interface between the Ω_1 and Ω_2 regions, which, when written in terms of the magnetic vector potential, takes the following form,

$$\vec{A}_1 = \vec{A}_2 \qquad \in \Omega_1 \cap \Omega_2 \tag{3}$$

$$\mu_1 \frac{\partial \vec{A}_1}{\partial n} = \mu_2 \frac{\partial \vec{A}_2}{\partial n} \qquad \in \Omega_1 \cap \Omega_2 \tag{4}$$

The thermal boundary conditions are rather simple and are written in terms of temperature as

$$T - T_1 = 0 \qquad \in \partial\Omega_{1,1} \tag{5}$$

$$-K \frac{\partial T}{\partial n} - q_2 = 0 \qquad \in \partial\Omega_{1,2} \tag{6}$$

with the second subscript differentiating the types of boundary conditions under consideration.

This paper considers 2-D and axisymmetric problems. Consequently, only one component of the vector potential survives. To facilitate computations, the co-ordinate system is chosen such that $\vec{A} = (0, 0, A\hat{z})$ is for a 2-D problem and $\vec{A} = (0, A\hat{\theta}, 0)$ for an axisymmetric problem.

For the problem illustrated in Figure 1, a natural choice for computational domains is to discretize the domain one Ω_1 by finite elements as detailed information on the induced electromagnetic field is required to calculate the needed Joule heating source distribution. Outside Ω_1, or, within the second domain Ω_2, which is filled with air, detailed information on local field distribution is unnecessary but the domain must be included as part of the computation because of the long range nature of the electromagnetic field. Thus for Ω_2, boundary elements will be employed to eliminate the need for the internal calculations.

3. Finite element formulation of vector potentials

First, we apply the finite elements to solve for the vector potential distribution inside the conducting workpiece, where there exists no external source. The vector potential equation may be more specifically written as,

$$\nabla^2 A = k^2 A + c\frac{A}{r^2} \qquad \in \Omega_1 \tag{7}$$

where c = 0 for a 2-D geometry and c = 1 for an axisymmetric system. The finite element formulation of equation (7) is straightforward. Following the variational approach[13], one obtains the integral representation of equation (7) as below,

$$\int_{\partial\Omega_1} r^c \frac{\partial A}{\partial n}\Phi d\Gamma - \int_{\Omega_1} r^c\left(\nabla A \bullet \nabla\Phi + \frac{c}{r^2}A\Phi + k^2 A\Phi\right)d\Omega = 0 \tag{8}$$

with $\partial\Omega_1 = \partial\Omega_{1,1} \cup \partial\Omega_{1,2}$.

By the Galerkin method, the vector potential distribution over an element may be assumed to take the following form,

$$A = \sum_{i=1}^{N_e} \Phi_i A_i \approx \Phi\mathbf{A} \tag{9}$$

where N_e is the number of nodes within the element.

Substituting equation (9) into equation (8) and performing the necessary numerical integration and standard finite element algebraic manipulations, one has

$$\mathbf{K}\mathbf{A} + \mathbf{N}_I\mathbf{q}_I = \mathbf{0} \tag{10}$$

where the coefficient matrices **K** and $\mathbf{N}_I$ are calculated by

$$K_{ij} = \int_{\Omega_e} \left(\nabla \Phi_i \cdot \nabla \Phi_j + c \Phi_i \Phi_j / r^2 + k \Phi_i \Phi_j \right) d\Omega \tag{11}$$

$$N_{I,ij} = \int_{\partial \Omega_I} r^c \Phi_i \Phi_j d\Gamma \tag{12}$$

Note that the matrix $\mathbf{N}_I$ represents the contribution from the interface between the finite element region and the boundary element region which is to be discussed next.

4. Boundary element formulation of vector potentials

We now apply the boundary elements to determine the vector potential in the exterior region, which is filled with air and consequently $k\vec{A} = 0$. There are applied current loops for electromagnetic field excitation. The vector potential distribution is governed by the following equation,

$$\nabla^2 \vec{A} = -\nabla \times \nabla \times \vec{A} = -\mu \vec{J} \qquad \in \Omega_2 \tag{13}$$

where we have made use of the Coulomb gauge or $\nabla \cdot \vec{A}$[28]·

To obviate the need for whole domain discretization of the exterior region, we seek a boundary element solution of equation (13). The Green function needed for this purpose must satisfy the following equation,

$$\nabla^2 \vec{G}(\mathbf{r}, \mathbf{r}') = -\nabla \times \nabla \times \vec{G}(\mathbf{r}, \mathbf{r}') = -\vec{\delta}(\mathbf{r}, \mathbf{r}') \tag{14}$$

where the vector Green function $\vec{G}$ = (0, 0, $G\hat{z}$) for a 2-D problem and $\vec{G}$ = (0, $G\hat{\theta}$, 0) for an axisymmetric problem.

Making use of vector Green's theorem[29,30] that relates the volume and surface integration of vector functions,

$$\iiint_V \left(\vec{G} \cdot \nabla \times \nabla \times \vec{A} - \vec{A} \cdot \nabla \times \nabla \times \vec{G} \right) dv = \oiint_S \left(\vec{A} \times \nabla \times \vec{G} - \vec{G} \times \nabla \times \vec{A} \right) \cdot d\vec{S} \tag{15}$$

Equations (13) and (14) can be combined to give a surface integral representation of the vector potential in the exterior region. On forming the dot product of $\vec{A}$ with equation (14) and of $\vec{G}$ with equation (13) and subtracting, followed by integration over the whole domain with respect to $\mathbf{r}'$, we have

$$\oiint_S \left(\vec{A} \times \nabla \times \vec{G} - \vec{G} \times \nabla \times \vec{A} \right) \cdot d\vec{S}(\mathbf{r}') = \iiint_V \left(-\vec{\delta}(\mathbf{r} - \mathbf{r}') \cdot \vec{A} + \mu \vec{J} \cdot \vec{G} \right) dv(\mathbf{r}') \tag{16}$$

The above equation holds true in general for magnetic vector potential induced by exciting coils. For either 2-D or axisymmetric vector potential under

consideration, the above vector formulation can be explicitly written in terms of its component form for any point $\mathbf{r} = \mathbf{r}_i$, viz.,

$$C(\mathbf{r}_i)A(\mathbf{r}_i) + \oint_{\partial\Omega_2} A(\mathbf{n}\bullet\nabla G)(2\pi r)^c d\Gamma = \oint_{\partial\Omega_2} G(\mathbf{n}\bullet\nabla A)(2\pi r)^c d\Gamma + \int_{\Omega_2} \mu J G(2\pi r)^c d\Omega \quad (17)$$

where $C(\mathbf{r}_i)$ is a geometric constant depending on whether point $\mathbf{r}_i$ is inside or on the boundary and also on the geometric characteristics of the boundary, and c = 0 for 2-D and c = 1 for axisymmetric problems. To simplify the notation, we have hereafter dropped the apostrophe on integration dummy variables. It is noted also that for axisymmetric problems integration has already been carried out over $\theta = 0$ to 2π.

Discretizing the boundaries of Ω_2 into small segments, as in the case for the finite element method, the boundary integrals in equation (17) can be re-written in terms of the integral contributions from individual boundary elements,

$$C(\mathbf{r}_i)A(\mathbf{r}_i) + \sum_{j=1}^{N} \int_{\partial\Omega_{2,j}} A(\mathbf{n}\bullet\nabla G)(2\pi r)^c d\Gamma_j = \sum_{j=1}^{N} \int_{\partial\Omega_{2,j}} G(\mathbf{n}\bullet\nabla A)(2\pi r)^c d\Gamma_j + \int_{\Omega_2} \mu J G(2\pi r)^c d\Omega \quad (18)$$

where N is the total number of boundary elements lying along the entire boundary of Ω_2. The above equation can be written for every boundary node, with the final result in terms of matrix form,

$$\mathbf{HA} = \mathbf{Gq} + \mathbf{F} \quad (19)$$

where **H** and **G** are the coefficient matrices, **A** and **q** the vector potential and flux vector at the boundary nodes respectively, and **F** represents the contribution from the current sources residing in Ω_2.

In the above boundary element formulation, the Green functions are different depending on whether or not the problem is 2-D or axisymmetric. For a 2-D vector potential problem, the Green function is the same as for a 2-D scalar potential[14] and is calculated by

$$G(\mathbf{r}_i, \mathbf{r}) = \frac{1}{2\pi} \ell n \frac{1}{|\mathbf{r}_i - \mathbf{r}|} \quad (20)$$

For an axisymmetric vector potential problem, however, the Green function is less well known. It may be derived from the consideration of a single current loop in free space[27,28] and the result takes the following form,

$$G(\mathbf{r}_i, \mathbf{r}) = \frac{1}{4\pi^2\sqrt{r_i r}} \left[\left(\frac{2}{\kappa} - \kappa \right) K(\kappa) - \frac{2}{\kappa} E(\kappa) \right] \quad (21)$$

where K(κ) and E(κ) are the elliptical integrals of the first and second kinds, respectively, and κ the geometric parameter. The calculation of G and its derivatives is lengthy and thus relegated to Appendix 1.

For either case, the coefficient C($\mathbf{r}_i$) can be calculated using the limiting process as detailed by Brebbia *et al.*[14]. With detailed derivation given in Appendix 2, the results are summarized as below for both 2-D and axisymmetric problems,

$$C(\mathbf{r}_i) = \begin{cases} 1 & \text{when } \mathbf{r}_i \text{ lies inside domain } \Omega_2 \\ \frac{1}{2} & \text{when } \mathbf{r}_i \text{ lies on a nonsmooth boundary } \partial\Omega_2 \\ (2\pi - \beta_1 - \beta_2)/2\pi & \text{when } \mathbf{r}_i \text{ lies on a nonsmooth boundary } \partial\Omega_2 \end{cases} \quad (22)$$

5. Coupling of finite and boundary elements

While there are many different ways to couple the boundary and finite element methods, the simplest and yet natural way is to make use of the physical constraints for the flux and field variables along the common boundaries of the FE and BE regions. This approach will be taken in this paper. For this purpose, equation (19) is re-written in terms of interface and non-interface boundary contributions,

$$[\mathbf{H}_I, \mathbf{H}_B] \begin{Bmatrix} \boldsymbol{A}_I \\ \boldsymbol{A}_B \end{Bmatrix} = [\mathbf{G}_I, \mathbf{G}_B] \begin{Bmatrix} \boldsymbol{q}_I \\ \boldsymbol{q}_B \end{Bmatrix} + \begin{Bmatrix} \boldsymbol{F}_I \\ \boldsymbol{F}_B \end{Bmatrix} \quad (23)$$

with subscript *I* denoting the interface quantities and *B* otherwise.

Through matrix manipulations, the unknown interface flux vector can be solved in terms of known variables and unknown interface potential vector along the interface,

$$\boldsymbol{q}_I = \mathbf{M}\boldsymbol{A}_I + \boldsymbol{F}_B \quad (24)$$

where $\boldsymbol{q}_I$ is the interface flux vector, $\boldsymbol{A}_I$ the interface potential vector, $\boldsymbol{F}_B$ the force vector resulting from known variables along the boundaries and $\mathbf{M}$ the resultant matrix.

Substituting equation (24) into equation (10), one has the final expression for the vector potential distribution within the finite element region,

$$\bar{\mathbf{K}}\bar{\boldsymbol{A}} = \bar{\boldsymbol{F}} \quad (25)$$

where $\bar{\boldsymbol{K}}$ is the resultant stiffness matrix, $\bar{\boldsymbol{A}}$ the unknown potential vector in the finite element region and $\bar{\boldsymbol{F}}$ the modified force vector which represents the effects of the heat source and known boundary conditions in both the finite element and boundary element regions.

The drawback of the direct implementation of the above approach is the direct inversion of matrix involved in obtaining equation (24). This also

destroys the original matrix structure and thus requires more memory space. One way to alleviate the problem is to inverse the matrix associated only with FE-BE interface nodes during the coupling and then solve the remaining boundary variables after the solution. The shortcoming with this method is that during the partial inversion process, matrix **H** (see below) has to be operated accordingly at the same time. We consider the following remedy for this problem in our actual implementation, through LU decomposition of the relevant matrix. This approach requires only subsequent operation of **H** and hence can be easily implemented in existing boundary element codes. Thus, if there have been FE and BE codes, only a simple subroutine module is needed to implement the coupling procedure.

Towards this, equation (23) is first rearranged so that other unknowns denoted by subscript B are placed below $\mathbf{q}_I$ and the known values are factored into the force vector. This would give rise to the following matrix equation,

$$[\mathbf{H}_I]\{A_I\} = [\mathbf{G}_I, \mathbf{G}'_B]\begin{Bmatrix} q_I \\ u_B \end{Bmatrix} + \begin{Bmatrix} F'_I \\ F'_B \end{Bmatrix} \tag{26}$$

where the said changes and rearrangements have been incorporated in $\mathbf{G}'$ and $\mathbf{F}'$. Next, matrix $\mathbf{G}$ ($\mathbf{G}_I$,$\mathbf{G}_B'$) is decomposed using the standard LU factorization, and the result is stored. Now $\mathbf{q}_I$ and $\mathbf{u}_B$ are solved in terms of $\mathbf{A}_I$ and $(\mathbf{F}'_I, \mathbf{F}'_B)^T$. This can be done readily for each column of the elements in $\mathbf{H}_I$ and also F.

For example, for the nth column of elements in HI, which is associated with the nth element of $\mathbf{A}_I$, the back-substitution is applied to obtain,

$$[\mathbf{G}]\begin{Bmatrix} \mathbf{q}^n{}_I \\ \mathbf{u}^n{}_B \end{Bmatrix} = \{\mathbf{H}^n{}_I\} \tag{27}$$

The procedure can be repeated for all the columns of $\mathbf{A}_I$ as matrix $\mathbf{G}$ has already been LU decomposed, and each of these operations will generate a solution of $(\mathbf{q}^n{}_I, \boldsymbol{u}^n{}_B)^T$. In comparison with equation (24), it is readily deduced that $\boldsymbol{q}^n{}_I$ is nothing but the nth column of elements in matrix **M**.

In incorporating the matrix equation equation (24) into the finite element formulation, the whole interface is treated as a macro boundary element for the finite element region, with its nodes coincident with those sitting on the FE-BE interface. This results in only a slight modification of calculation of skyline profile structure of the final finite element matrix, but allows equation (24) to be easily assembled into the final global matrix $\bar{\mathbf{K}}$.

6. Treatment of corners in the boundary element region

In using the boundary element method for the solution of boundary value problems, the corners of the discretized region require special treatment as fluxes or potentials can be discontinuous around the corners. There are in general four techniques to treat the discontinuity around a corner:

(1) rounded corners;

(2) discontinuous elements;

(3) double nodes; and

(4) double fluxes.

In our studies, these four techniques were all examined and the double flux method was found to be the easiest to use and also give accurate results. Results of compatible accuracy can also be obtained by placing discontinuous boundary elements around a corner but the procedures of implementation can be very tedious. Consequently, the double flux method was used for all results presented in this paper.

Our numerical experience indicated that corner discontinuity along the common boundary between the finite element and boundary element regions must also be treated carefully if accurate results are to be obtained. Typically, at such a corner, the potential must be continuous as seen from equation (3) but the normal derivatives are discontinuous from one side of the corner to the other (see Figure 2). The double flux method was used also to treat these corners. The idea may be briefly described below. Referring to Figure 2, the gradient of potential may be calculated from the tangential derivatives along the FE-BE interface,

$$\frac{\partial A}{\partial r} = \frac{1}{\sin(\alpha_2 - \alpha_1)}\left(\frac{\partial A}{\partial t_1}\sin\alpha_2 - \frac{\partial A}{\partial t_2}\sin\alpha_1\right) \tag{28}$$

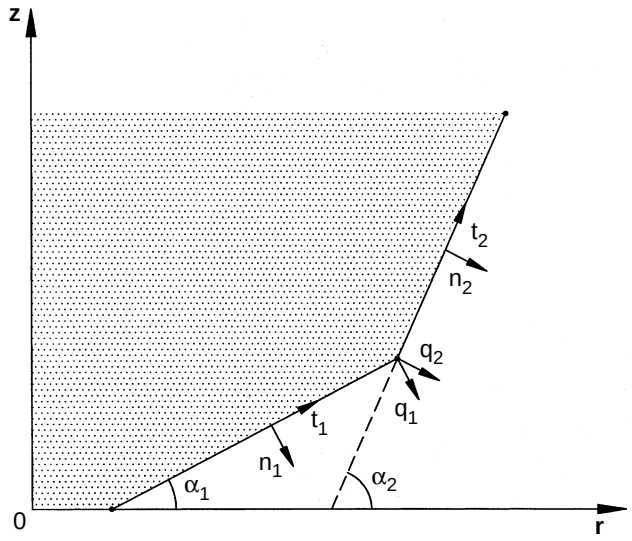

Figure 2.
Double flux treatment of corners associated with the interface of finite element and boundary element regions

$$\frac{\partial A}{\partial z} = \frac{1}{\sin(\alpha_2 - \alpha_1)}\left(\frac{\partial A}{\partial t_2}\cos\alpha_1 - \frac{\partial A}{\partial t_1}\cos\alpha_1\right) \tag{29}$$

where $\partial A/\partial t_i$ (i = 1, 2) is the tangential derivative and $\mathbf{t}_i = (\cos\alpha_i, \sin\alpha_i)$ the tangential unit vector.

With these two equations, the normal derivatives can be calculated by,

$$\nabla A \cdot n_1 = \frac{\partial A}{\partial n_1} = \frac{1}{\sin(\alpha_2 - \alpha_1)}\left(\frac{\partial A}{\partial t_1}\cos(\alpha_2 - \alpha_1) - \frac{\partial A}{\partial t_2}\right) \tag{30}$$

$$\nabla A \cdot n_2 = \frac{\partial A}{\partial n_2} = \frac{1}{\sin(\alpha_2 - \alpha_1)}\left(\frac{\partial A}{\partial t_1} - \frac{\partial A}{\partial t_2}\cos(\alpha_2 - \alpha_1)\right) \tag{31}$$

where $\mathbf{n}_i = (\sin\alpha_i, -\cos\alpha_i)$ is the normal unit vector associated with either side of the corner. As the tangential derivatives can be calculated using the finite difference of the potentials at the adjacent nodal points, the normal derivatives can thus be obtained as a function of the nodal potentials. This can be readily factored into the global matrices generated by the coupled boundary and finite element formulations.

7. Finite element formulation of temperature field

The finite element solution of the thermal field, as described by equation (2), is well established[13]. The final matrix representation of the finite element solution of equation (2) may be written as

$$M_T\frac{d\mathbf{T}}{dt} + K_T\mathbf{T} = \mathbf{F}_T \tag{32}$$

where the matrices and force vectors are calculated by

$$M_{ij,T} = \int_{\Omega_e}\rho C_p\Phi_i\Phi_j d\Omega \tag{33}$$

$$K_{ij,T} = \int_{\Omega_e}K\nabla\Phi_i\cdot\nabla\Phi_j d\Omega \tag{34}$$

$$F_{i,T} = \int_{\Omega_e}0.5\omega\sigma\vec{A}\cdot\vec{A}^*\Phi_i d\Omega + \int_{\partial\Omega_e}\Phi_i K\frac{\partial T}{\partial n}d\Gamma \tag{35}$$

In calculating the Joule heating contribution in **F** term, the vector potential is interpreted at the Gaussian integration points over a finite element.

8. Results and discussion

The coupled finite element and boundary element algorithm described above is now applied to predict the induced electromagnetic field and temperature field in conducting samples surrounded by alternating current loops. Three case studies are presented in this section to illustrate the application of the algorithm developed.

Case 1: A metallic sphere surrounded by a single current loop

In this first example, the FE/BE program is tested against available solutions for the electromagnetic field and temperature field computations over a simple geometry. We consider a single current loop surrounding a conducting sphere. The loop is located at the equator plane. For this simple geometry, the induced magnetic vector potential Aϕ can be calculated analytically and written for a spherical coordinate system (r, ϕ, θ) it becomes[11],

$$A_\phi = \frac{\mu I \sin \nu}{2}\left(\frac{a}{r}\right)^{1/2} \sum_{n=1}^{\infty} \frac{2n+1}{n(n+1)}\left(\frac{a}{r_o}\right)^n \frac{P_n^1(\cos \nu) P_n^1(\cos \theta) I_{n+1/2}(kr)}{kaI_{n-1/2}(ka)} \quad (36)$$

where I_k is the modified Bessel function of the first kind and P_n^1 the associated Legendre polynomials[31].

Figure 3 shows the comparison of results of the vector potential obtained from the numerical model and from the analytical solution given above. The calculation used 808 4-node finite elements and 36 2-node boundary elements. The mesh for the finite element region is shown in Figure 4. It is apparent from the figure that the numerical results are in excellent agreement with analytical solution for both the real and imaginary parts of the vector potential. The FE/BE code has also been compared with solutions for 2-D slab and infinitely long cylinders and gratifying agreement between the numerical and analytical results was also obtained[32].

Figure 5 shows the Joule heating distribution within the sphere. Clearly, near the current loop the Joule heating attains a maximum value and decays rapidly both in the θ- and r-directions away from the current loop, which is consistent with the predictions from the electromagnetic theory. The temperature contour calculated for this problem using the FE-BE numerical model described above is given in Figure 6. The Joule heating effects are clearly manifested in the region adjacent to the current loop. The analytical solution for the temperature distribution is also available for this case[11]. The comparison of the numerical results and the analytical solutions once again is gratifying, as appears in Figure 7.

It is important to note that because of the small skin depth (0.67mm) associated with the problem, caution must be exercised to employ finite element meshes to obtain solutions with reasonably good accuracy. A small error in the calculation of magnetic vector potential can result in significant error in the subsequent temperature calculations. With the availability of the analytical

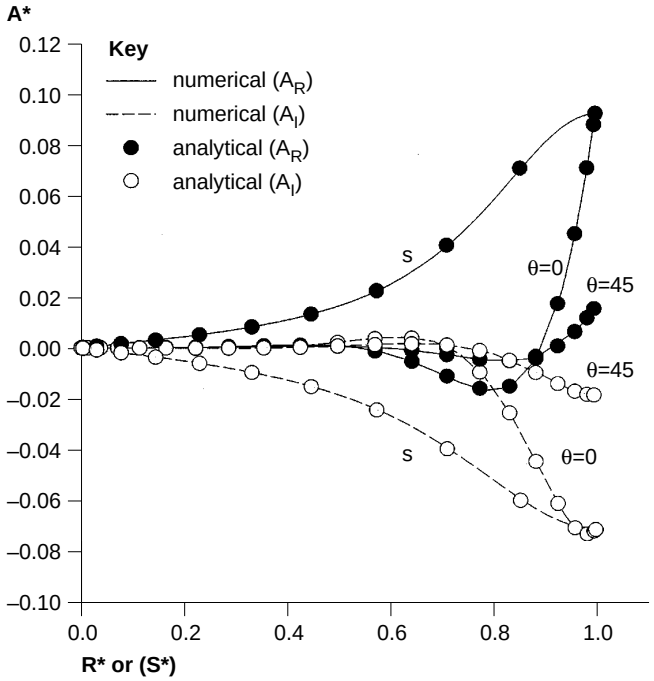

Figure 3.
Comparison of numerical and analytical results for the radial and surface distribution of the vector potential at different θ angles.

S refers to the vector potential distribution along the surface measured from $\theta = 0$ to $\theta = \pi/2$. A_R and A_1 refer to real and imaginary parts of the vector potential A. $R^* = r/a$, $S^* = s/(a\pi)$ and $A^* = 2A/\mu I$. The conditions used are: coil current I (peak) = 212 amp, frequency = 1.45×10^5Hz, radius of sphere (a) = 6mm, radius of coil loop = 9mm, convective heat transfer coefficient = 60.6 W.k–m^2, electrical conductivity = 3.85×10^6 1/(Ohm-m), and thermal conductivity = 135.9 W/K–m

solution for this problem this numerical aspect can be assessed more effectively. For this purpose, many different types of meshes and approximations were investigated using the FE-BE code. Our numerical experience showed that if uniform meshes were applied, about 1,400 or more 4-node elements need to be used in the finite element region in order to get an accuracy of 1×10^{-4} (relative error) in comparison with the analytical solutions. With progressive decreasing meshes, where dense mesh is placed near the surface and progressively coarser meshes applied away from the surface, the number of the elements used for the calculation can be substantially reduced. For the same accuracy of 1×10^{-4}, only 400 4-node elements, as shown in Figure 4, are needed. Further studies showed that for exponentially decaying meshes, intended to follow the decaying behavior of the electromagnetic field within the skin depth near the surface, results are the same. Other options of element approximation were also tested. With the same number of nodes but using quadratic elements (9-node or 8-node elements for the finite element region and 3-node elements for the boundary element region), no

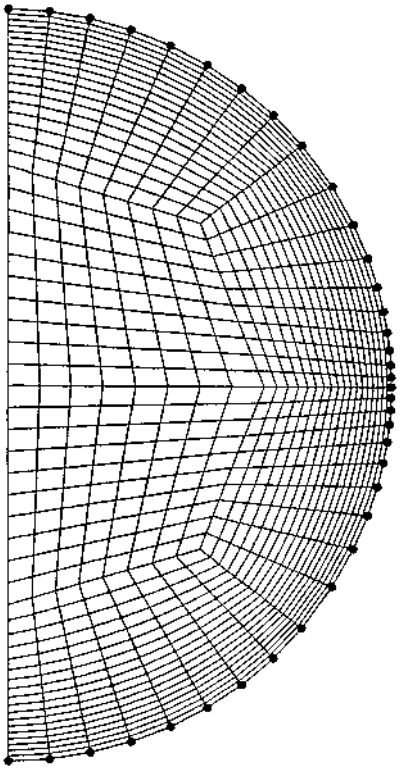

Figure 4. The mesh of the finite element region used for the results in Figure 3. Note that the boundary element nodes for this particular case become the interface nodes between the FE and BE regions. The infinity boundary conditions are incorporated into the boundary element formulation directly, as described in [14]

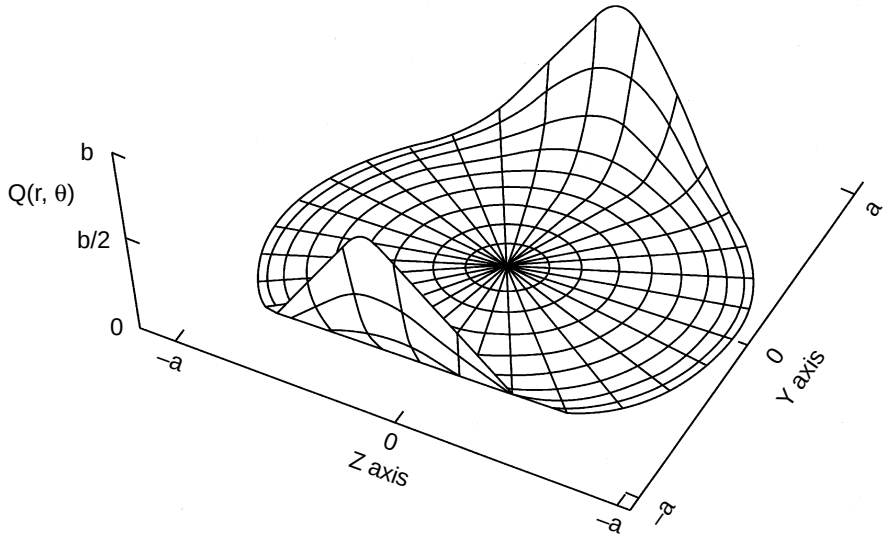

Figure 5. 3-D view of Joule heating distribution. The conditions are the same as in Figure 3 and b is 4×10^6 J/m^{3}s

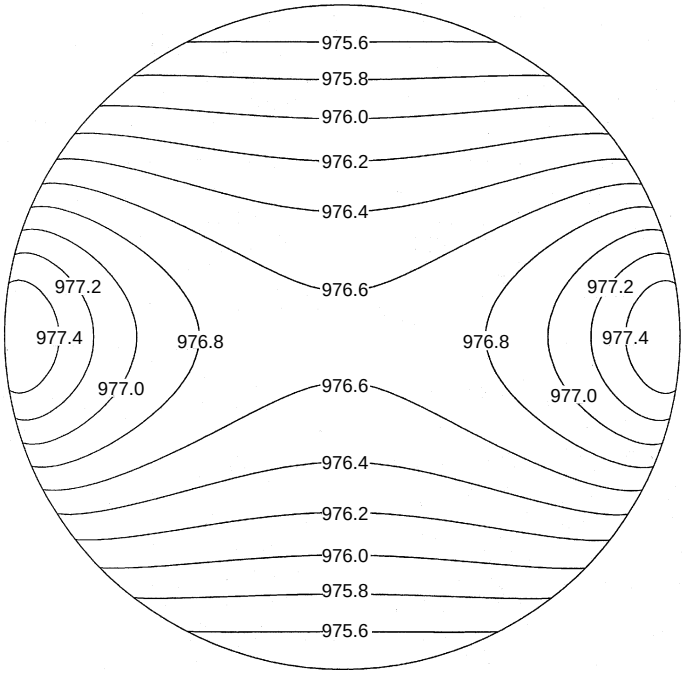

Figure 6.
The temperature contour solution. The conditions are the same as in Figure 3

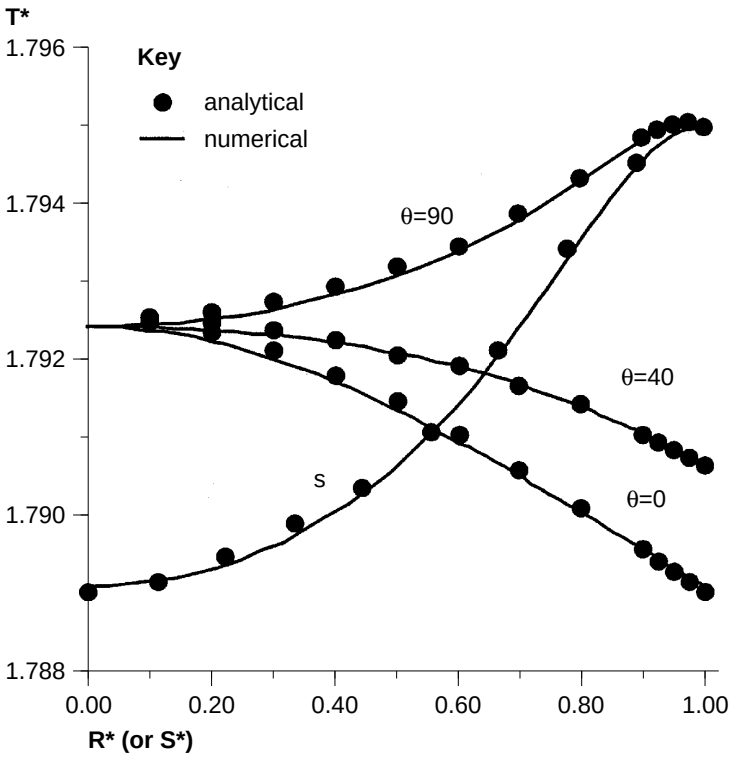

Figure 7.
The comparison of numerical results and the analytical solutions. The conditions are the same as in Figure 3. $T^* = (T-298)K/\mu\omega l^2$)

improvement in accuracy has been found and in fact the results are slightly less accurate than 4-node elements. From all the numerical experiments that were carried out, 4-node elements, with their size distribution following an increasing geometric progression at a ratio of 1.3 inward from the surface, provide the best accuracy with a relative error of 1×10^{-4} for this problem.

Case 2. Induction heating of a Ni sphere by a set of current loops

The system to be studied for this case is illustrated in Figure 8, which has been used currently for the laser-based thermal property measurements[33]. In this system, the sphere is inductively heated by surrounding coils to a fixed temperature. The FE-BE numerical algorithm is used to provide an estimate of the time needed for heating up and also the temperature distribution within the sphere. The calculation started with a prediction of electromagnetic field distribution in terms of the vector potential and then the temperature is calculated with the Joule heating as a source. The surface of the sphere is assumed to lose heat to the surroundings by thermal radiation. The nonlinearity associated with radiation boundary condition is treated using the simple successive substitution method. Figures 9 and 10 contrast the steady state temperature distributions for two different current conditions. The former is for the case where the top and bottom sets of the coils are at the same polarity, while the later for the case in which the two sets are out of phase by 180. Clearly, the spatial distribution and the magnitude of the temperature in the sphere are completely different for the two conditions considered. For Figure 9, the profile closely resembles the one as if it were produced by a coil placed around the equator of the sphere (see also Figure 6). On the other hand, the temperature distribution for the case of Figure 10 suggests as if it were produced by two coils, with opposite polarity, symmetrically placed over the equator plane. It is noticed that minimum temperature occurs near the equator, in contrast with Figure 9 where the maximum temperature occurs at the same location. These

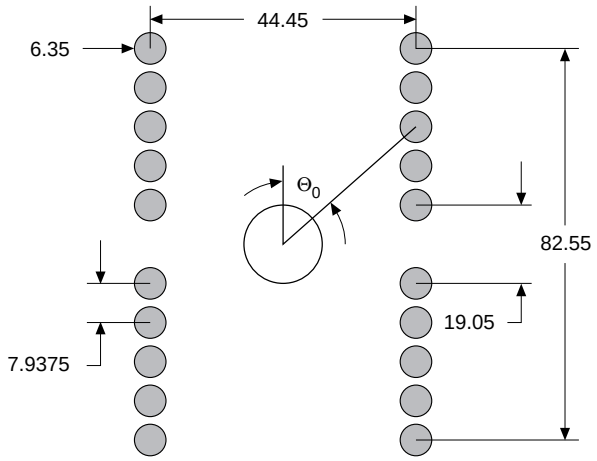

Figure 8.
The system studied in case 2. Under the conditions: coil current (rms) = 200 amps, coil frequency = 450kHz, density = 8,900.0kg/m^3, radius of spherical specimen = 6.35mm, reference temperature = 298K, emissivity = 0.14 to 0.17

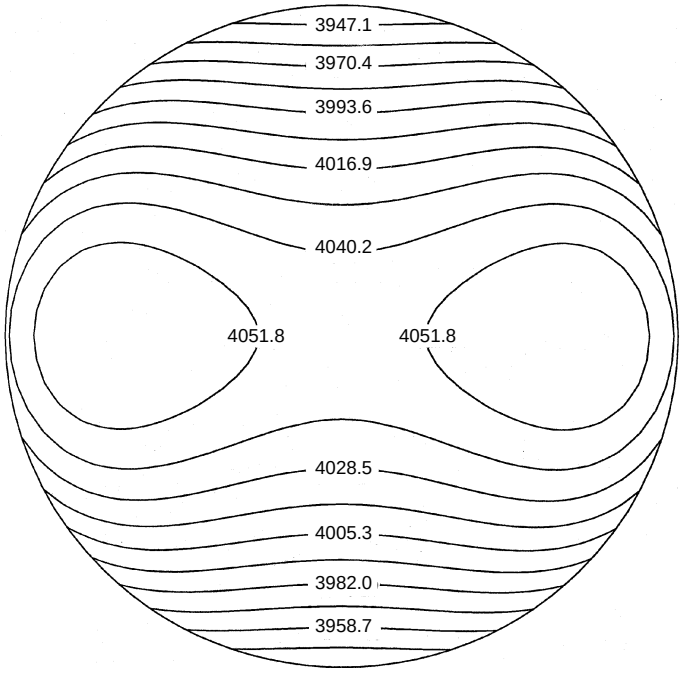

Figure 9.
The steady state temperature distribution for the case where the upper and lower sets of the coils are of the same polarity. The conditions are the same as in Figure 8

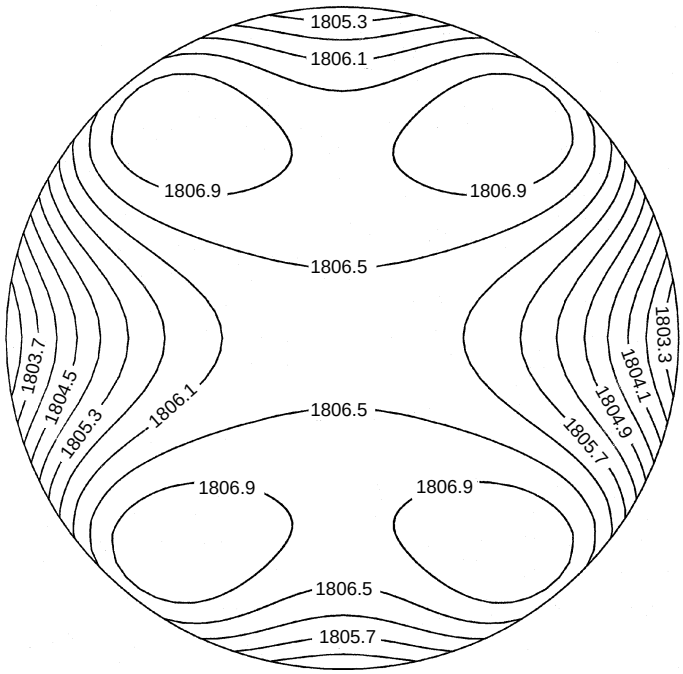

Figure 10.
The steady state temperature distribution for the case where the upper and lower sets of the coils are of the same polarity. The conditions are the same as in Figure 8

results should not come as a surprise in that the top and bottom sets of coils produce an additive effect for Figure 9 but cancel out each other for Figure 10.

For the purpose of thermal property measurements, the sphere is often heated to a certain temperature of interest, not necessarily the steady state. Information on temperature evolution, both spatial and transient, can be of critical importance. Figure 11 plots a set of temperature contours at different time steps for the system, with the top and bottom sets of coils set at opposite polarities. Apparently, the temperature evolves spatially as the heating continues. Radiation boundary condition is again used for the simulation and the sphere is allowed to be heated until its center reaches a temperature of 100K below melting point. The total time needed to reach the desired temperature is 809 seconds, which compares with 50 seconds when the top and bottom coil sets are in phase.

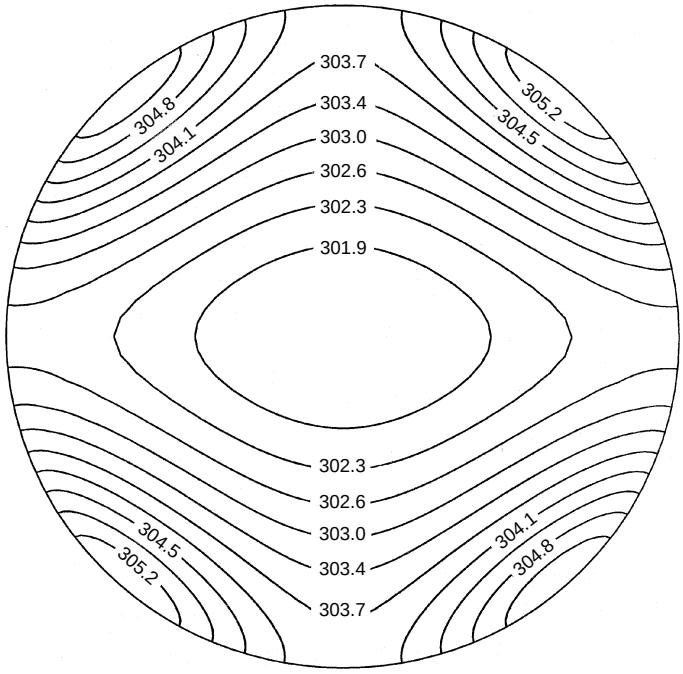

Figure 11.
Snapshots of temperature contours at different time steps (a: 2.0 secs, b: 130 secs; c: 386 secs, and d: 674 secs) for the system. The conditions are the same as in Figure 8

Case 3. Temperature distribution in a deformed droplet supported by levitation coils

In this third case, the temperature distributions within a deformed droplet is considered. The coil geometry and locations are illustrated in Figure 12. This set of the coils produced desired magnetic forces to support the metallic sphere and also the needed Joule heating energy to melt it. The system has been widely

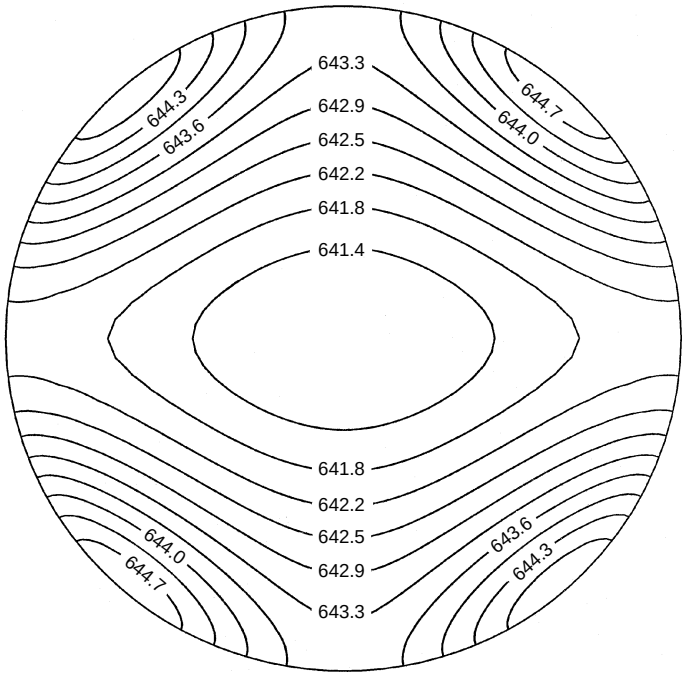

Figure 12.
The configuration and dimensions of the coil for case 3. The calculations were processed for 1.5gm aluminium droplet with the following conditions: coil current (rms) –240 Amps, frequency –218kHz and emissivity –0.3

used for laboratory studies of solidification phenomena and has recently been modified for measuring thermal and fluid properties of conducting liquids of high melting temperatures under microgravity conditions[12]. The deformation of the sphere occurs as a result of the balance between the electromagnetic, gravitational and surface tension forces. The flow induced force, or hydrodynamic force, makes only a slight contribution, and thus may be ignored as a first approximation. The FE-BE code is combined with a deforming-mesh based algorithm to calculate the droplet shape for this case.

The computation involves iterative solution of the electromagnetic field and the free surface shape and is detailed by the same authors in [32]. The final shape along with the steady state temperature distribution, as calculated by the FE-BE coupling method, is shown in Figure 13. Again the heat loss is assumed to be due to the surroundings at a temperature of 298K through radiation. For this case, we see that maximum temperature occurs near the bottom of the droplet and there exists no symmetry over the equator plane of the droplet because of gravity effects.

Concluding remarks

This paper has presented a coupled finite element and boundary element computational methodology for the solution of magnetothermal problems. The finite element formulation, boundary element formulation and their coupling as

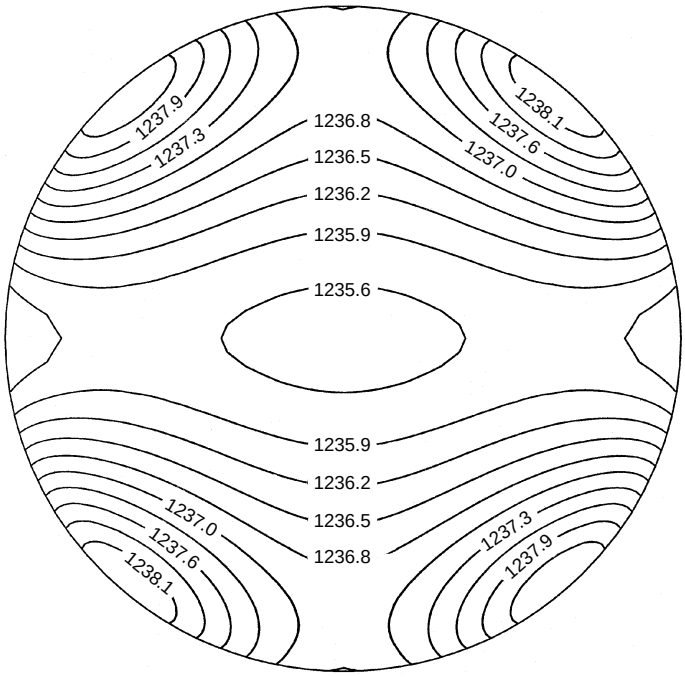

Figure 13.
The steady state temperature distribution calculated by the FE-BE coupling method for the droplet. The conditions are the same as in Figure 12

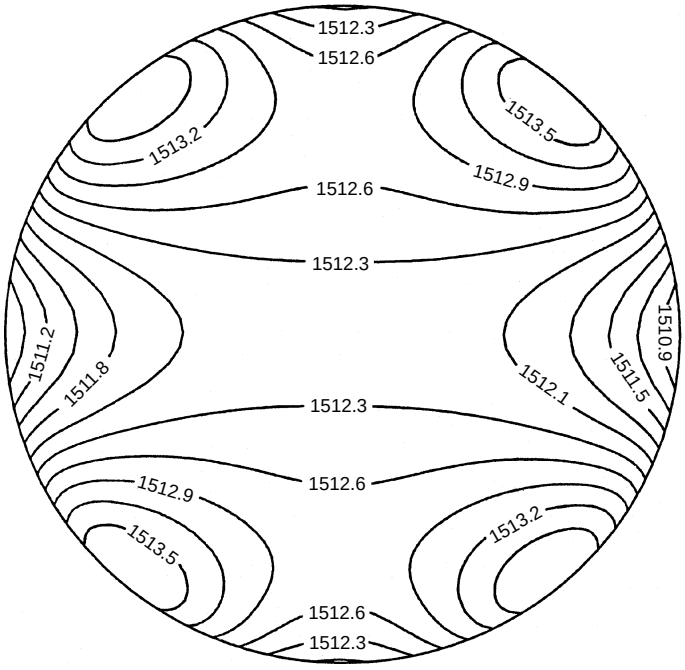

Figure 14.

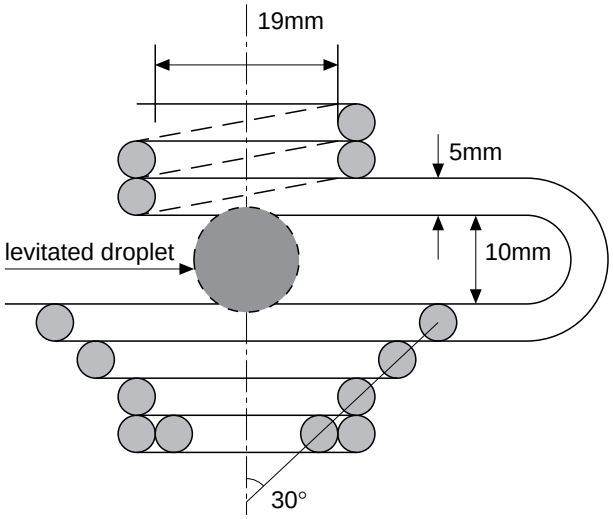

Figure 15.

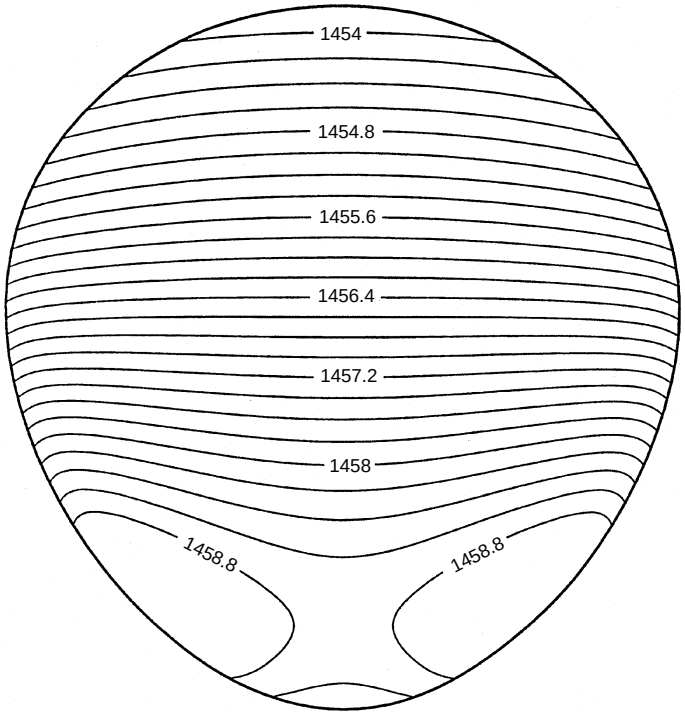

Figure 16.

well as their implementation procedures are discussed. Corners for both FE-BE interface and BE regions, where discontinuous fluxes exist, are treated using the double flux concept. Numerical results are presented for three different systems and compared with analytical solutions when available. Numerical experiments suggest that for magnetothermal problems involving small skin depths, a careful mesh distribution is critical for accurate prediction of the field variables of interest. It is found that the accuracy of the thermal calculation is strongly dependent upon that of the magnetic vector potential. A small error in the magnetic vector potential can produce significant errors in the subsequent temperature calculations. Thus, particular attention must be made in order to design a suitable mesh for accurate prediction of vector potentials. From all the cases examined, 4-node linear elements with adequate progressive coarsening of meshes from the surface gave the results with best accuracy.

References

1. Tarapore, E.D. and Evans, J.W., "Fluid velocities in induction furnaces, part I: theory and laboratory experiments", *Met. Trans. B*, Vol. 7, 1976, p. 343.
2. Tarapore, E.D., Evans, J.W. and Langfeldt, J., "Fluid velocities in induction furnaces, Part II: large scale measurements and predictions", *Met. Trans. B*, Vol. 8, 1977, p. 179.
3. Szekely, J. and Chang, C.W., "Turbulent electromagnetically-driven flow in metals processing", *Ironmaking & Steelmaking,* Vol. 3, 1977, pp. 190-204.
4. Li, B.Q., Evans, J.W. and Cook, D.P., "An improved mathematical model for electromagnetic casters and testing by a physical model", *Metall. Trans.* B., Vol. 22, 1991, pp. 121-34.
5. Evans, J.W., Cook, D.P. and Nishioka, S., "Mathematical and physical modeling of electromagnetically supported melts in three dimensions", in Szekely, J., Evans, J.W., Balzek, K. and El-Kaddah, N. (Eds), *Magnetohydrodynamics in Process Metallurgy*, TMS/AIME, Warrendale, PA, 1992, pp. 35-44.
6. El-Kaddah, N., "The magnetic suspension process", in Szekely, J., Evans, J.W., Balzek, K. and El-Kaddah, N. (Eds), *Magnetohydrodynamics* in *Process Metallurgy*, TMS/AIME, Warrendale, PA, 1992, pp. 283-9.
7. Riahi, D.N. and Walker, J.S., "Float zone shape and stability with electromagnetic body force due to a radio-frequency induction coil", *Journal of Crystal Growth,* Vol. 94, 1989, pp. 635-42.
8. Pang, S.S., Van Beek, G.A. and Lea, R.H., "Development of an advanced electrically conductive fiber reinforced plastics pipe", *Polymer Composites*, Vol. 16 No. 5, 1995, pp. 409-14.
9. Zong, J-H., Li, B.Q. and Szekely, J., "The electrodynamic and hydrodynamic phenomena in magnetically-levitated droplets, Part I, steady state behavior", *Acta Astronautica*, Vol. 26 No. 6, 1992, pp. 435-49.
10. Natarajan, T.T. and El-Kaddah, N., "Calculation of the electromagnetic field and melt shape in electromagnetic confinement systems: a comparison between numerical methods", in Voller, V.R., March, S.P. and El-Kaddah, N. (Eds), *Materials Processing in the Computer Age II*, TMS/AIME, Warrendale, PA, 1995, pp. 255-65.
11. Li, B.Q., "The magnetothermal phenomena in electromagnetic levitation processes", *Int. J. Eng. Sci,* Vol. 31 No. 2, 1993, pp. 201-20.
12. Zong, J-H, Li, B.Q. and Szekely, J., "The electrodynamic and hydrodynamic phenomena in magnetically-levitated droplets, Part II, transient behavior and heat transfer considerations", *Acta Astronautica*, Vol. 29 No. 4, 1993, pp. 305-11.
13. Zienkiewicz, O.C. and Taylor, R.L., *The Finite Element Method,* 4th Ed., McGraw-Hill, New York, NY, 1988.

14. Brebbia, C.A, Telles, J.C.F. and Wrobel, L.C., *Boundary Element Techniques: Theory and Applications in Engineering*, Springer-Verlag, New York, NY, 1984.
15. Li, B.Q. and Evans, J.W., "Boundary element solution of heat convection-diffusion problems", *J. Comp. Phys.*, Vol. 93 No. 2, 1991, pp. 255-72.
16. Li, B.Q. and Evans, J.W., "Computation of shapes of electromagnetically supported menisci in electromagnetic casters, Part II: calculations in three dimensions", *IEEE Transactions on Magnetics*, Vol. 25 No. 7, 1991, pp. 4443-8.
17. Song, S. and Li, B.Q., "Coupled boundary/finite element solution of thermal and electrodynamic problems in materials processing", in Voller, V.R., March, S.P. and El-Kaddah, N. (Eds), *Materials Processing in the Computer Age II*, 243-254, TMS/AIME, Warrendale, PA, 1995.
18. Zienkiewicz, O.C., Kelly, D.W. and Bettess, P., "The coupling of the finite element method and boundary solution methods", *Int. J. Numer. Methods Eng.*, Vol. 11 No. 2, 1977, pp. 355-75.
19. Beer, G., "BEFE – coupled boundary element finite element computer program," *Adv. Eng. Software*, Vol. 6 No. 2, 1983, pp. 103-9.
20. Beer, G., "Finite element, boundary element and coupled analysis of unbounded problems in elastostatics", *Int. J. Numer. Methods Eng.*, Vol. 19, 1983, pp. 567-80.
21. Krishnamurthy, T. and Raju, I.S., "Coupling finite and boundary element methods for two dimensional potential problems", *Int. J. Numer. Methods Eng.*, Vol. 36, 1993, pp. 3595-616.
22. Salon, S.J. and Schneider, J.M., "A hybrid finite element – boundary integral formulation of Poisson's equation", *IEEE Trans. on Magnetics*, Vol. 17 No. 6, 1981, pp. 2574-6.
23. Lynch, D.R.,Paulsen, K.D., "Hybrid element method for unbounded electromagnetics problems in hyperthermia", *Int. J. Numer. Methods Eng.*, Vol. 23, 1986, pp. 1915-37.
24. Salon, S.J. and Peng, J.P., "Hybrid finite – element boundary solutions to axisymmetric scalar potential problems", in Cendes, Z.J. (Ed.), *Computational Electromagnetics*, 1986, pp. 251-61.
25. Hong, C.P., Umeda, T. and Kimura, Y., "Numerical models for casting solidification: Part I. the coupling of the boundary element and finite difference methods for solidification problems", *Metall. Trans. B.*, Vol. 15, 1984, pp. 91-9.
26. Reddy, J.N. and Gartling, D.K., *The Finite Element Method in Heat Transfer and Fluid Dynamics*, CRC Press, Boca Raton, FL, 1994.
27. Smythe, W.R., *Static and Dynamics Electricity*, Chapter 10, McGraw-Hill, New York, NY, 1968.
28. Jackson, J.D., *Classical Electrodynamics*, John Wiley & Sons, New York, NY, Chapter 2-6, 1972.
29. Morse, P. and Fashback, H., *Methods of Theoretical Physics*, McGraw-Hill, New York, NY, 1953.
30. Tsai, C-T., *Dyadic Green's Functions in Electromagnetic Theory*, Intext Educational Publishers, San Francisco, CA, Chapter 1, 1971.
31. Abramowitz, M. and Stegun, I.A., *Handbook of Mathematical Function*, US Government Printing Office, Washington, DC, 1964.
32. Song, S.P. and Li, B.Q., "Computation of magnetically-supported free surface by a coupled finite/boundary element method", *EPD Congress-96*, 1964.
33. Shen, F., Khodadadi, J.M., Woods, M.C., Weber, J.K.R. and Li, B.Q., "Containerless thermal diffusivity determination of levitated spherical specimen by an external flash method: theory and experimental verification", *Journal of Heat Transfer* (accepted).
34. Buktov, E., *Mathematical Physics*, Addison-Wesley Publishing Company, Menlo Park, CA, Chapter 6, 1968.

Appendix 1. Derivation of the axisymmetric vector Green function and its derivatives

The axisymmetric vector Green function used for vector potential calculations may be derived by making use of the vector potential generated by a single current loop[27,28]. To facilitate the derivation, we write the current loop in terms of a single ring source of current density, **J**. For a current element with a length of ds along the current flow direction in space as shown in Figure A1, the law of charge conservation reads as follows,

$$\mathbf{J}\delta(\mathbf{x}-\mathbf{x}')dv = I\delta(\mathbf{x}-\mathbf{x}')d\mathbf{s} = I\delta(\mathbf{x}-\mathbf{x}')d\mathbf{x} \tag{A1.1}$$

Integration along the current path gives

$$\mathbf{J} = I\oint_{\Gamma}\delta(\mathbf{x}-\mathbf{x}')d\mathbf{x} \tag{A1.2}$$

In the spherical coordinate system under consideration as shown in Figure A1, the current loop assumes axisymmetry and hence **x** or the current path is only a function of ϕ,

$$\mathbf{x}(\phi) = a\sin\theta(\cos\phi\mathbf{i} + \sin\phi\mathbf{j}) + a\cos\theta\mathbf{k} \tag{A1.3}$$

and d**x** becomes

$$d\mathbf{x}(\phi) = a\sin\theta(-\sin\phi\mathbf{i} + \cos\phi\mathbf{j})d\phi = a\sin\theta\mathbf{i}_{\phi}d\phi \tag{A1.4}$$

The Dirac delta function in a spherical coordinate system is defined as[29]

$$\delta(\mathbf{x}-\mathbf{x}') = \frac{\delta(\rho-\rho')\delta(\cos\theta-\cos\theta')\delta(\phi-\phi')}{J(x,y,z/\rho,\cos\theta,\phi)} = \rho^{-2}\delta(\rho-\rho')\delta(\cos\theta-\cos\theta')\delta(\phi-\phi') \tag{A1.5}$$

where $J(x, y, z/\rho, \cos\theta, \phi)$ is the Jacobian.

Substituting in the definition of **J** (equation (A1.2) and integrating gives,

$$\begin{aligned}\mathbf{J}(\mathbf{x}') &= I\sin\theta a^{-1}\delta(a-\rho')\delta(\cos\theta-\cos\theta')\mathbf{i}_{\phi'}\\ &= I\sin\theta' a^{-1}\delta(\rho'-a)\delta(\cos\theta'-\cos\theta)\mathbf{i}_{\phi'}\end{aligned} \tag{A1.6}$$

where we have used the condition, $\delta(\alpha-\rho') = \delta(\rho'=a)$[34].

Now consider a vector potential function that satisfies the following partial differential equation,

$$\nabla^2\left(A^*_{\phi}\mathbf{i}_{\phi}\right) = -\mu J_{\phi}\mathbf{i}_{\phi} \tag{A1.7}$$

the solution of which can be written in terms of a volume integral[28],

$$A^*_{\phi}\mathbf{i}_{\phi} = -\frac{\mu}{4\pi}\int\frac{J_{\phi}(\mathbf{x}')\mathbf{i}_{\phi}(\mathbf{x}')dv'}{|\mathbf{x}-\mathbf{x}'|}$$

where

$$|\mathbf{x}-\mathbf{x}'| = \sqrt{\rho^2+\rho'^2-2\rho\rho'(\cos\theta\cos\theta'+\sin\theta\sin\theta'\cos(\phi-\phi'))}. \tag{A1.8}$$

The volume integral can be simplified dramatically if we recognize the fact that A^*_ϕ is independent of ϕ because of the axisymmetry of the problem. This allows us to arbitrarily select ϕ without affecting the final result. With this we then have,

$$A^*_\phi = \frac{\mu I}{4\pi}\int_0^a\int_{4\pi}\frac{\sin\theta'\,\delta(\rho'-a)\delta(\cos\theta'-\cos\theta'')\cos\phi'\,\rho'^2\,d\rho'\,d\Omega'}{a\left(\rho^2+\rho'^2-2\rho\rho'(\cos\theta\cos\theta'+\sin\theta\sin\theta'\cos\phi')\right)^{1/2}}$$

$$= \frac{\mu I a}{4\pi}\int_0^{2\pi}\frac{\cos\phi'\,d\phi'}{\left(\rho^2+a^2-2a\rho\sin\theta\cos\phi'\right)^{1/2}}$$

$$= \frac{\mu}{\pi}\frac{Ia}{\sqrt{a^2+\rho^2+2ar\sin\theta}}\left[\frac{(2-k^2)K(k)-2E(k)}{k^2}\right] \tag{A1.9}$$

where $d\Omega' = \sin\theta'\,d\theta'\,d\phi'$ is the solid angle, $\cos\theta'' = 0$ as seen in Figure A1, and the argument of the elliptic integrals is given by,

$$k^2 = \frac{4a\rho\sin\theta}{a^2+\rho^2+2a\rho\sin\theta} \tag{A1.10}$$

For A^*_ϕ to be used as the Green function, it needs to satisfy the following governing equation,

$$\nabla^2\left(G\mathbf{i}_\phi\right) = -\delta(\mathbf{x}-\mathbf{x}')\mathbf{i}_\phi \tag{A1.11}$$

Comparison with equation (A1.7) shows that

$$\delta(\mathbf{x}-\mathbf{x}')\mathbf{i}_\phi = c\mu J_\phi\mathbf{i}_\phi \qquad \text{and} \qquad G = cA^*_\phi \tag{A1.12}$$

The constant c is determined by the condition required on the delta function,

$$1 = \int\delta(\mathbf{x}-\mathbf{x}')dv$$

$$= \int_0^r\int_{-1}^{1}\int_0^{2\pi} c\mu I\sin\theta a^{-1}\delta(\rho-a)\delta(\cos\theta-\cos\theta')\rho^2 d\rho d\cos\theta d\phi$$

$$= c\mu I a 2\pi \tag{A1.13}$$

With this and also writing the result in terms of cylindrical co-ordinates (see Figure A1), the desired Green function then is derived from equation (A1.9). To be consistent with equation (22), we need to take $\mathbf{r} = \mathbf{r}$ (r = a, z) as the source point and $\mathbf{r}_i = \mathbf{r}_p$ (r_i, z_i) as the observation point. Thus, we have the Green function for the axisymmetric vector potential,

$$G(\mathbf{r}_i,\mathbf{r}) = G(r_i,z_i;r,z) = \frac{1}{4\pi^2\sqrt{r_i r}}\left[\left(\frac{2}{k}-k\right)K(k)-\frac{2}{k}E(k)\right] \tag{A1.14}$$

or equation (22) in the text with

$$k^2 = \frac{4r_i r}{\left(r_i+r\right)^2+\left(z_i-z\right)^2} \tag{A1.15}$$

The normal derivative of G can now be readily calculated. From equation (A1.14), one has

$$\frac{\partial G}{\partial n} = \frac{\partial G}{\partial r} n_r + \frac{\partial G}{\partial z} n_z$$

$$= \frac{k n_r}{8\pi^2 \sqrt{r_i r}} \left\{ \frac{(z_i - z)^4 + (z_i - z)^2 (2r_i^2 + r^2) + r_i^2 (r_i^2 - r^2)}{\left[(z_i - z)^2 + (r_i - r)^2 \right] r_i r^2} E(k) - \frac{(z_i - z)^2 + r_i^2 + r^2}{r_i r^2} K(k) \right\}$$
$$+ \frac{k n_z}{8\pi^2 \sqrt{r_i r}} \left[\frac{(z_i - z)^2 + r_i^2 + r^2}{(z_i - z)^2 + (r_i - r)^2} E(k) - K(k) \right] \frac{z_i - z}{r_i r} \qquad \text{(A1.16)}$$

where use has been made of the following relations[31],

$$k \frac{dK(k)}{dk} = \frac{E(k)}{(1 - k^2)} - K(k) \qquad \text{and} \qquad k \frac{dE(k)}{dk} = E(k) - K(k)$$

For the convenience of numerical computations, the complete elliptic integrals may be approximated by the following polynomials,

$$K(m) = \left[a_0 + a_1 m_1 + \ldots + a_4 m_1^4 \right] + \left[b_0 + b_1 m_1 + \ldots + b_4 m_1^4 \right] \ell n \left(1/m_1 \right) + \varepsilon(m);$$

$$|\varepsilon(m)| \leq 2 \times 10^{-8} \qquad \text{(A.17)}$$

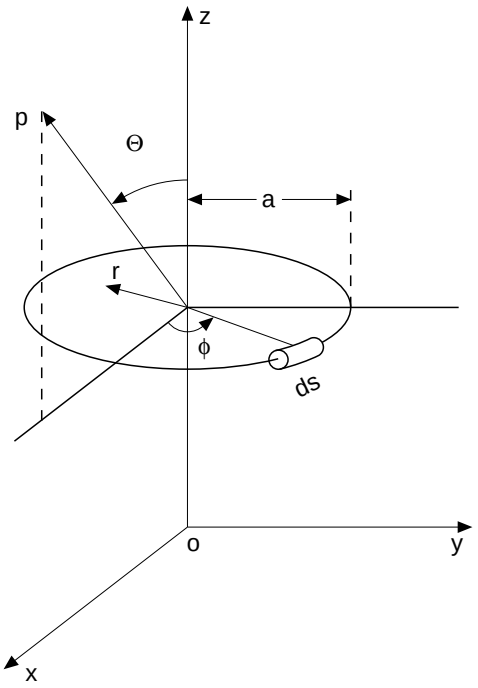

Figure A1. Single current coil geometry and co-ordinate system used for the derivation of axisymmetric Green function and its derivatives for magnetic vector potential

and

$$E(m) = \left(c_0 + c_1 m_1 + \ldots + c_4 m_1^4\right) + \left(d_1 m_1 + \ldots + d_4 m_1^4\right) \ell n\left(1/m_1\right) + \varepsilon(m)$$

$$|\varepsilon(m)| \leq 2 \times 10^{-8} \quad \text{(A1.18)}$$

where $m = k^2$ and $m_1 = 1 - m$.

Appendix 2. Evaluation of $C(\mathbf{r}_i)$ for the BE solution of axisymmetric vector potentials:

The calculation of the term $C(\mathbf{r}_i)$ arising from the boundary element formulation may be carried out using the limiting process. For 2-D problems, $C(\mathbf{r}_i)$ has been derived for both smooth and non-smooth boundaries[14]. The similar procedure is now applied to obtain the coefficient for vector axisymmetric problems. If $\mathbf{r}_i$ is inside the integration domain, $C(\mathbf{r}_i)$ is readily calculated from the definition of the Delta function, leading to

$$C(\mathbf{r}_i)A(\mathbf{r}_i) = \iiint_V \delta(\mathbf{r}_i - \mathbf{r}')A(\mathbf{r}')dv(\mathbf{r}') = A(\mathbf{r}_i) \quad \text{or} \quad C(\mathbf{r}_i) = 1 \quad \text{for } \mathbf{r}_i \text{ within } \Omega \quad \text{(A2.1)}$$

When $\mathbf{r}_i$ lies along the boundary of computational domain, $\partial\Omega_2$, $C(\mathbf{r}_i)$ needs to be calculated using the limiting process. To do that, the boundary is altered to include $\mathbf{r}_i$ in the domain by constructing a small curve of radius ε around the point r_i, as shown in Figure A2. The term involving the delta function is the same as above. On taking the limiting process or $\varepsilon \to 0$, one additional boundary term will arise and contribute to $C(\mathbf{r}_i)$[14], i.e.:

$$C(\mathbf{r}_i) = 1 + \lim_{\varepsilon \to 0} 2\pi \int_{\Gamma_\varepsilon} \frac{\partial G}{\partial n(\mathbf{r})} r d\Gamma(\mathbf{r}) = 1 + \lim_{\varepsilon \to 0} 2\pi \int_{-\beta_1}^{\beta_2} \frac{\partial G}{\partial n(\mathbf{r})} r \varepsilon d\beta \quad \text{(A2.2)}$$

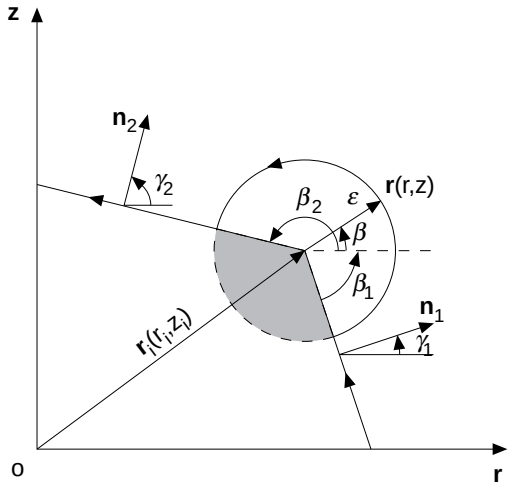

Figure A2.
Geometric definition of variables and co-ordinate system used for the calculation of coefficient $C(\mathbf{r}_i)$ associated with boundary element formulation

From Figure A2, there exist the following geometric relations,

$$n_r = \cos\beta \qquad \text{and} \qquad n_z = \sin\beta$$

$$\varepsilon^2 = |\mathbf{r}_i - \mathbf{r}| = (r_i - r)^2 + (z_i - z)^2$$

$$r - r_i = \varepsilon\cos\theta \qquad \text{and} \qquad z - z_i = \varepsilon\sin\theta$$

In addition, the following asymptotic behavior exists for the elliptic functions and the relevant parameters as $\varepsilon \to 0$,

$$E(k) \to 1; \qquad K(k) \to \ell n(8R/\varepsilon); \qquad \text{and} \qquad k \to 1$$

With the above substituted into equation (A1.16) and then equation (A2.2), and upon eliminating higher order terms, the coefficient C($\mathbf{r}_i$) can be calculated by,

$$\begin{aligned} C(\mathbf{r}_i) &= 1 + \lim_{\varepsilon\to 0} 2\pi \int_{-\beta_1}^{\beta_2} \frac{1}{8\pi^2 r_i}\left(\frac{-2r_i\cos\beta - \varepsilon\ell n(8r_i/\varepsilon)}{\varepsilon R}\cos\beta - \frac{\sin^2\beta}{\varepsilon}\right) r\varepsilon d\beta \\ &= 1 + \lim_{\varepsilon\to 0} \frac{1}{4\pi} \int_{-\beta_1}^{\beta_2} -2\left(\cos^2\beta + \sin^2\beta\right) d\beta \\ &= \frac{1}{2\pi}(2\pi - \beta_2 - \beta_1) \end{aligned} \qquad \text{(A2.3)}$$

or equation (23) in the text. The physical meaning of C($\mathbf{r}_i$) is now clear. It represents the contribution of the portion of the source that lies within the domain, as indicated by the shaded area. For a smooth boundary, $\beta_1 + \beta_2 = \pi$ and hence C($\mathbf{r}_i$) = 1/2.